Chemical
Science

EDGE ARTICLE

View Article Online
View Journal | View Issue

Check for updates

Cite this: *Chem. Sci.*, 2019, **10**, 8323

All publication charges for this article have been paid for by the Royal Society of Chemistry

A symbiotic hetero-nanocomposite that stabilizes unprecedented $CaCl_2$-type TiO_2 for enhanced solar-driven hydrogen evolution reaction†

Yuelan Zhang,[a] Liping Li,*[a] Yan Liu,[a] Tao Feng,[a] Shibo Xi,[b] Xiyang Wang,[a] Chenglin Xue,[a] Jingyu Qian[c] and Guangshe Li*[a]

Received 12th March 2019
Accepted 22nd July 2019

DOI: 10.1039/c9sc01216h

rsc.li/chemical-science

Symbiotic hetero-nanocomposites prevail in many classes of minerals, functional substances and/or devices. However, design and development of a symbiotic hetero-nanocomposite that contains unachievable phases remain a significant challenge owing to the tedious formation conditions and the need for precise control over atomic nucleation in synthetic chemistry. Herein, we report a solution chemistry approach for a symbiotic hetero-nanocomposite that contains an unprecedented $CaCl_2$-type titania phase inter-grown with rutile TiO_2. $CaCl_2$ structured TiO_2, usually occurring when bulk rutile-TiO_2 is compressed at an extreme pressure of several GPa, is identified to be a distorted structure with a tilt of adjacent ribbons of the *c*-axis of rutile. The structural specificity of the symbiotic $CaCl_2$/rutile TiO_2 hetero-nanocomposite was confirmed by Rietveld refinement, HRTEM, EXAFS, and Raman spectra, and the formation region ($TiCl_4$ concentration *vs.* reaction temperature) was obtained by mapping the phase diagram. Due to the symbiotic relationship, this $CaCl_2$-type TiO_2 maintained a high stability *via* tight connection by edge dislocations with rutile TiO_2, thus forming a $CaCl_2$/rutile TiO_2 heterojunction with a higher reduction capacity and enhanced charge separation efficiency. These merits endow symbiotic $CaCl_2$/rutile TiO_2 with a water splitting activity far superior to that of the commercial benchmark photocatalyst, P25 under simulated sunlight without the assistance of a cocatalyst. Our findings reported here may offer several useful understandings of the mechanical intergrowth process in functional symbiotic hetero-nanocomposites for super interfacial charge separation, where interfacial dislocation appears to be a universal cause.

Introduction

Symbiotic hetero-nanocomposites prevail in many classes of minerals, functional substances and/or devices,[1–3] providing opportunities to maximize interfacial/surface chemical reactions and synergistic effects between components essential for important applications. Important applications of these hetero-nanocomposites have been witnessed in a variety of fields, including catalysis, photovoltaic conversion, energy storage, decontamination, and clean energy production since these nanocomposites are merited by optimum interfacial/surface chemical reactions and synergistic effects of components.[4–8] Depending on the interconnection of each component through van der Waals forces or covalent bonds and on the interplay of individual components, heterogeneous composites could always generate a superior performance. For example, strong interfacial interactions in between components enable charge transfer within heterogeneous composites, accounting for the effective separation of photo-generated electrons and holes through interfaces for excellent photocatalytic overall water splitting activities.[9–14] When noble metals are strongly supported onto oxides in forming heterogeneous composites, excellent CO oxidation ability was achieved because of the simultaneous CO adsorption of noble metals and oxygen activation of MO_x.[15–17] Indeed, when growing nanocomposites or epitaxial oxide films, pronounced interfacial interactions could be possible because of the interfacial dislocations that directly influence the average stress and strain states in the composites,[18] while upon cooling down from the growth temperature, tensile strain is stored in the composites or films (owing to the thermal expansion mismatch between component oxides) which could stabilize certain highly useful, but also barely accessible phases under ambient conditions.[19] All these demonstrate a great possibility of using interfacial dislocations or strains in developing symbiotic hetero-nanocomposites that

---

[a] State Key Laboratory of Inorganic Synthesis and Preparative Chemistry, College of Chemistry, Jilin University, Changchun 130012, P. R. China. E-mail: lipingli@jlu.edu.cn

[b] Institute of Chemical and Engineering Sciences, A*STAR, 1 Pesek Road, Jurong Island, Singapore 627833, Singapore

[c] State Key Laboratory of Supramolecular Structure and Materials, College of Chemistry, Jilin University, Changchun 130012, P. R. China

† Electronic supplementary information (ESI) available. See DOI: 10.1039/c9sc01216h

contain unachievable phases for many important applications, which however remains a significant challenge owing to the tedious formation conditions (like pre-synthesis and post-processing) and the need for precise control over atomic nucleation in synthetic chemistry. Consequently, it is highly necessary to explore one-step approaches for synthesizing symbiotic hetero-nanocomposites *via* precise control over the composition intergrowth during the nucleation and crystallization process.

Depending on the synthetic chemistry, symbiotic hetero-nanocomposites could be achieved in many classes of oxide systems because of the intrinsic nature of polymorphs. For instance, TiO_2 has many crystalline phases. Heterogeneous composites formed in between rutile, anatase, and/or brookite-type TiO_2 have been evidenced (*e.g.*, anatase/rutile, anatase/brookite, rutile/brookite or anatase/rutile/brookite) to show strong interfacial interactions because of the intergrowth of these phases during the synthesis of TiO_2. Closely related to the specific combination of these constituent structures, heterogeneous composites have found a broad range of applications such as in photocatalysis, lithium-ion batteries, CO oxidation, and ammonia synthesis.[17,20–22] P25 is a typical heterogeneous composite that consists of anatase and rutile at a molar ratio of 79 to 21, and has shown a preeminent performance in photocatalytic hydrogen production and sewage treatment. Indeed, the intergrowth compositions of TiO_2 are rather limited to those of common phases, while heterogeneous composites that involve many other unconventional phases of TiO_2 (like TiO_2-H, $CaCl_2$ phase, or α-PbO_2 phase, *etc.*) are barely accessible. This is because the synthesis of these unconventional phases can only be achieved under harsh experimental conditions such as high pressure and high temperature, even though these phases have been predicted to have superior activity in batteries and photocatalysis.[23,24] Consequently, an intergrowth of heterogeneous composites with those unconventional phases is highly important, but also fairly challenging.

We hold the opinion that the $CaCl_2$ phase and rutile could most probably form a symbiotic hetero-nanocomposite with a broad impact if successful. We took $CaCl_2$/rutile as the target to study based on the following considerations: (i) among all unconventional phases of TiO_2, the orthorhombic $CaCl_2$-type TiO_2 polymorph with a space group of *Pnnm* is a distorted structure of tetragonal rutile with a relative tilt of adjacent ribbons about the *c*-axis, whose structure is very close but absolutely different from rutile. They are likely to connect with each other and grow together through orientation attachment, leading to dislocations in between them that could in turn stabilize this metastable phase; (ii) although the $CaCl_2$ phase can only be synthesized under high pressure by assistance of foreign ions currently,[25,26] solution chemistry especially the hydrothermal approach merited by a special subcritical reaction medium and abundant intermediate states could regulate the flexible reaction procedure to obtain several special phases with a metastable structure. Further, hydrothermal methods allow control over the nucleation and growth processes essential for synthesizing symbiotic hetero-nanocomposites with strong interactions.[27] (iii) There are many other rutile counterparts like SnO_2, SiO_2, GeO_2, and RuO_2 that have been found to transform into the $CaCl_2$ structure under high pressure.[28–31] Thus, once such a solution methodology was established, one may expect more opportunities to develop other $CaCl_2$/rutile symbiotic hetero-nanocomposites. As we all know, rutile is an excellent multi-functional material in a wide range of fields, and thus it is highly possible for symbiotic hetero-nanocomposites with a distorted rutile structure to show superior performances that have not yet been accessible.

Herein, we successfully synthesized a symbiotic hetero-nanocomposite that consists of metastable $CaCl_2$ structured TiO_2 and rutile TiO_2 *via* a mild solution chemistry approach. The composite structure of symbiotic $CaCl_2$/rutile TiO_2 was confirmed by XRD data refinement, EXAFS, and Raman spectra. Then, the phase diagram for the symbiotic hetero-nanocomposite was depicted based on the reactant concentration and reaction temperature, in which the $Ti(OH)_2(OH_2)_4{}^{2+}$ saturation ion played a crucial role. Despite the presence of metastable $CaCl_2$ structured TiO_2, the as-prepared hetero-nanocomposite showed a high stability and a superior performance in photocatalytic H_2 evolution reactions through forming a type II heterojunction. This work provides insights into developing new methods for synthesizing high-performance symbiotic hetero-nanocomposites that contain metastable compounds.

Results and discussion

Titania polymorphs in this work were synthesized through a high-acidity hydrothermal process utilizing $TiCl_4$ as the titanium source, and no other reagents were needed except for the aqueous solution. After reaction at 120 °C for 2 h, the product was examined by powder X-ray diffraction (XRD) to identify the structure. As shown in Fig. 1c, the XRD data of the product were readily indexed to a rutile phase of TiO_2 in tetragonal structure (JCPDS no. 21-1276). However, unlike the traditional rutile TiO_2, the diffraction line (110) around two theta of 28° is clearly asymmetric (Fig. 1a). This diffraction peak could be fitted well using two Lorentz fitting peaks: one shifted towards a higher diffraction angle, while the other one shifted oppositely and became symmetric gradually after calcination at 200 °C and 400 °C (Fig. S1† and 1b). Typically, the origins of the doublet peaks are regarded as $K_{\alpha1}$ and $K_{\alpha2}$ rays of the Cu target during XRD measurements. However, the peak splitting caused by the Cu target couldn't be so large.[32] Thus, the influence of the instrument was excluded, and the peak splitting around two theta of 28° could be attributed to the change of the structure. To the best of our knowledge, the peak splitting of diffraction peaks could be the consequences of (i) strain; for instance, polymer capping induced strain may result in changes in the lattice constant, and crystal boundary strain in the twin crystal could give rise to doublet XRD peaks;[33–35] (ii) surface species, such as water vapour on the surface of ice;[36] and (iii) distortion of the structure.[37] Asymmetry of diffraction peaks induced by strain and surface species is often composed of one strong intrinsic peak accompanied by weak peaks at the shoulder, differing from two comparative peaks. The sole possibility is appearance of the composition in a new phase. Firstly, we assumed that the

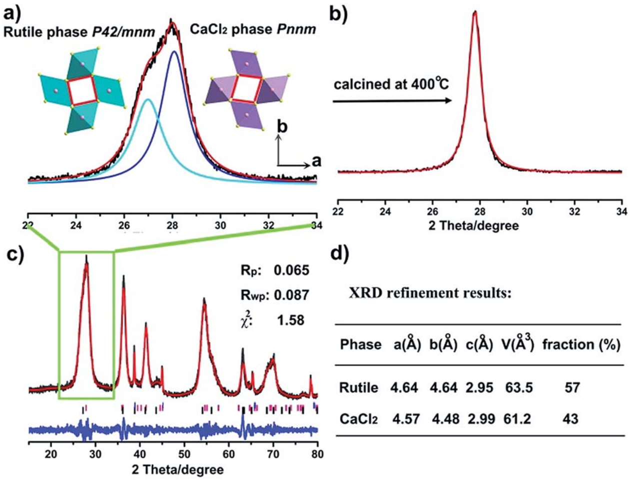

Phase	a(Å)	b(Å)	c(Å)	V(Å³)	fraction (%)
Rutile	4.64	4.64	2.95	63.5	57
CaCl2	4.57	4.48	2.99	61.2	43

Fig. 1 Structural analyses by X-ray diffraction (XRD) refinement: (a) XRD pattern of the enlarged peak (110) for $CaCl_2$/rutile TiO_2. Inset illustrates the crystal structures for rutile TiO_2 and $CaCl_2$ phase TiO_2. (b) XRD pattern of the calcined product $CaCl_2$/rutile-400. (c) Rietveld structural data refinement results for $CaCl_2$/rutile TiO_2. Black, red, and blue curves represent the experimental diffraction data, calculated data, and deviation between the experimental and calculated data, respectively. The vertical bars below the pattern denote the standard diffraction data for internal standard Al (blue), rutile TiO_2 (black) and $CaCl_2$ phase TiO_2 (rose red). (d) The structural refinement results for components rutile and $CaCl_2$ in the composite.

peak splitting originates from two rutile TiO_2 phases intergrown with a shrinking lattice and an expanded lattice. That is, two tetragonal TiO_2 structures with space group of $P4_2/mnm$ coexist in this material. Thus, according to eqn (S1),† two sets of lattice parameters could be obtained when calculated using d values of peaks (110) and (101), as shown in Table S1.† The lattice volume obtained from the left peak (peak 1) is well consistent with the experimental curve of V–1/D of rutile TiO_2, while the lattice volume obtained from the right peak (peak 2) severely deviates from the curve (Fig. S2†), giving a hint that peak 2 does not originate from rutile TiO_2 with a contracted lattice. This means that one has to look for other structured TiO_2 similar to rutile. Coincidentally, a similar phenomenon has been found in rutile SnO_2 under a pressure of 250 bar, and the author assigned the structure to a $CaCl_2$ structure (space group $Pnnm$) that forms through a second-order phase transition from the rutile phase.[38] Typically, the $CaCl_2$ structure is an orthorhombic structure that occurs at a very high pressure, which has been found in many rutile structured compounds including SnO_2, SiO_2, GeO_2, RuO_2, TiO_2, *etc.*[25,28–31] It seems reasonable that there is a $CaCl_2$ phase in the as-prepared TiO_2, which explains the peak splitting around two theta of 28° in Fig. 1a. Thus, the XRD patterns were fitted in terms of rutile and $CaCl_2$ structure. As one expected, the results agree well with the data (Fig. 1, Tables 1, S2 and S3†). The lattice parameters of the $CaCl_2$ structure in $CaCl_2$/rutile TiO_2 were determined to be a = 4.57 Å, b = 4.48 Å, c = 2.99 Å. It is authentic to identify the existence of $CaCl_2$-type structured TiO_2 in $CaCl_2$/rutile TiO_2.

In order to further verify our speculation, $CaCl_2$/rutile TiO_2 was further characterized by field-emission scanning electron microscopy (SEM) and transmission electron microscopy (TEM) which display a cone shape at a dimension of about 2–3 μm (Fig. 2b and S6†). The cone was composed of numerous nanorods with a width of about 5 nm grouped by small nanoparticles through orientation attachment growth. High resolution transmission electron microscopy (HRTEM) indicates that the lattice spacing is ordered locally, while the lattice parameters vary in different parts (Fig. 2c, f and g). The interplanar spacing (d) in different parts of Fig. 2c differ (such as $d_1 = 0.320$ Å, $d_2 = 0.328$ Å), which are in accordance with the plane (110) in rutile and $CaCl_2$ structure from the refinement results of $CaCl_2$/rutile TiO_2 (Table 1). Besides that, there are a large number of dislocations in the joint point of both parts (Fig. 2c). Benefitting from the dislocation, the neighbouring particles attached to each other and tended to grow together, as illustrated in the schematic diagram in Fig. 2a. Thus, the formation of $CaCl_2$-type structured TiO_2 intergrown with rutile TiO_2 was confirmed.

When the intergrowth structure was calcined at high temperatures, the lattice tends to be regular and transformed entirely into a rutile TiO_2 phase with a little shrinkage relative to the rutile phase in $CaCl_2$/rutile TiO_2. This observation is likely due to the phase transition of the metastable $CaCl_2$ structure to the rutile structure and the growth of crystals. The d spacing could be identified to decrease to a value of 0.325 Å from HRTEM, which is also consistent with XRD refinement results of $CaCl_2$/rutile-400 and commercial rutile (Fig. S3 and S4, Tables S4 and S5†). It should be mentioned that uniform mesopores (~8 nm) appeared with the cone-shape maintained after calcination (Fig. 2d and S6b†), in line with the pore distributions obtained by N_2 adsorption/desorption isotherm curves (Fig. S5†). Lattice rearrangement should be responsible for the appearance of mesopores. As the calcination temperature increased, the specific areas decreased (Table S6†) due to the grain growth.

The Raman spectrum is often used as a fingerprint to analyze the symmetry and structural order. As shown in Fig. 3a, three signals located at about 140, 400, and 600 cm^{-1} are associated with the modes B_{1g}, E_g, and A_{1g} of the rutile TiO_2 lattice,

Table 1 XRD refinement results of the samples

Sample name (phase)	Lattice	Space group	a/Å	b/Å	c/Å	V/Å^3	d(110)/Å	χ^2
$CaCl_2$/rutile TiO_2 ($CaCl_2$ phase)	Orthorhombic	*Pnnm*	4.569	4.484	2.988	61.21	3.200	1.575
$CaCl_2$/rutile TiO_2 (rutile phase)	Tetragonal	$P4_2/mnm$	4.642	4.642	2.947	63.51	3.283	
$CaCl_2$/rutile-400 (rutile phase)	Tetragonal	$P4_2/mnm$	4.596	4.596	2.957	62.46	3.250	5.513
Ref.TiO_2 (rutile phase)	Tetragonal	$P4_2/mnm$	4.593	4.593	2.958	62.42	3.248	2.542

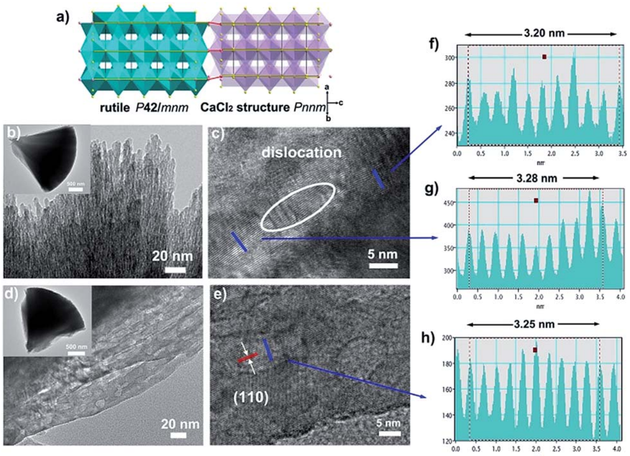

Fig. 2 Morphology and assembly structure of the composite: (a) schematic diagram of the assembly structure, (b) TEM and (c) HRTEM images for $CaCl_2$/rutile TiO_2. (d) TEM and (e) HRTEM images for $CaCl_2$/rutile-400. Profiles of lattice fringes for (f and g) $CaCl_2$/rutile TiO_2 in different areas; and (h) profiles of lattice fringe for $CaCl_2$/rutile-400. Scale value in insets of (b) and (d) are 500 nm.

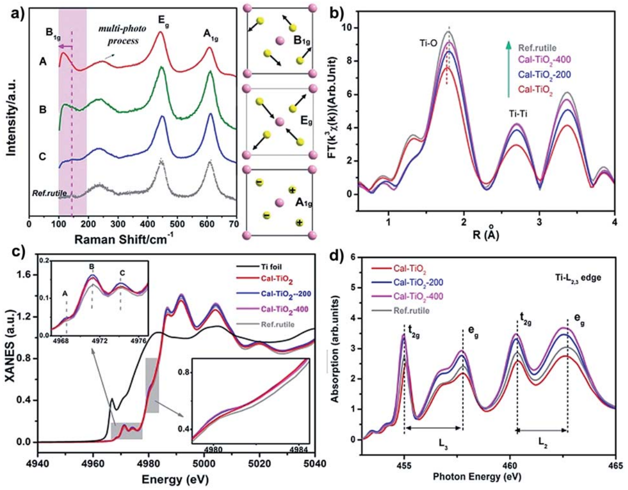

Fig. 3 Structural information from Raman and EXAFS. (a) Raman spectra, (b) R-space Fourier-transformed FT ($k^3\chi(k)$) of Ti K-edge EXAFS, (c) XANES spectra of the Ti K-edge and (d) Ti $L_{2,3}$-edge of the samples $CaCl_2$/rutile TiO_2 (A), $CaCl_2$/rutile-200 (B), $CaCl_2$/rutile-400 (C) and commercial rutile TiO_2. The gray area in (c) highlights the pre-edge region.

respectively, while that at 200 cm^{-1} can be assigned to the multi-phonon modes of rutile TiO_2.[39,40] It should be pointed out that in $CaCl_2$/rutile TiO_2, a weak signal of the B_{1g} mode for rutile TiO_2 at 140 cm^{-1} became inconspicuous and overlapped by a new peak at about 110 cm^{-1}. In Raman active modes of rutile, the central cation Ti is silent, and the Raman modes are purely O vibrations.[39] As shown in the schematic diagram in Fig. 3a, the oxygen ions vibrate perpendicular to the Ti–O bond in the B_{1g} mode. Typically, the B_{1g} mode is highly sensitive to the long-range order of TiO_2 crystals and softens significantly more than other modes under high pressures.[41] The Raman shift in rutile often has a relationship with the strain, O/Ti ratio, size effect, O isotope, and volume effect, which usually give rise to several wavenumber shifts.[39,40,42,43] The most significant factor could be the pressure-induced-volume effect as represented by a shift of about 20 cm^{-1} softened at 6 GPa.[40] Several viewpoints have attributed the origin of anomalistic softening in the B_{1g} mode to a thermal/pressure-induced-lattice contraction or an incipient structural phase transition, which explains well the softening of mode B_{1g}. Thus, the new emerging peak at 110 cm^{-1} most likely originates from $CaCl_2$ structured TiO_2 in $CaCl_2$/rutile TiO_2. Due to the intense signal of this vibration, the intrinsic signal for rutile is covered by that of $CaCl_2$ phase TiO_2.

In order to investigate the coordination environment of $CaCl_2$/rutile TiO_2, Ti K-edge X-ray adsorption spectra of $CaCl_2$/rutile TiO_2 and its calcined samples were measured and compared. As shown in Fig. 3b, Ti K-edge EXAFS of $CaCl_2$/rutile TiO_2, $CaCl_2$/rutile-200, $CaCl_2$/rutile-400, and commercial rutile TiO_2 (Ref.rutile) are transformed into the radial distribution function *via* R-space Fourier-transformed FT ($k^3\chi(k)$). The first peak at about 1.8 Å is attributed to the six Ti–O bonds in the first coordination sphere (TiO_6 octahedron) and the second peak at about 2.7 Å could be ascribed to Ti–Ti distances of these samples. The third peak at 3.4 Å corresponds to Ti–O bonds at about 3.5 Å and Ti–Ti bonds at 3.57 Å. Obviously, the Ti–O distance in $CaCl_2$/rutile TiO_2 is shorter than those of other samples, which could be caused by $CaCl_2$-type structured TiO_2 with a contracted unit cell. Normalized Ti K-edge XANES spectra are shown in Fig. 3c. The line shape of $CaCl_2$/rutile TiO_2, $CaCl_2$/rutile-200 and $CaCl_2$/rutile-400 is similar to that of commercial rutile TiO_2 except for a subtle change in the relative intensities of peaks and the absorption edge. The three major features in the pre-peaks of the Ti K-pre-edge region are labelled A, B, and C, which are identified to be associated with hybridized Ti 3d–4p, and 1s → $2t_{2g}$ and 1s → $3e_g$ transitions, respectively.[44,45] The intensity of pre-peak B in $CaCl_2$/rutile TiO_2, $CaCl_2$/rutile-200, and $CaCl_2$/rutile-400 is stronger than that of commercial rutile TiO_2. It is well established that the intensity of pre-peak B enhanced with increasing concentration of defects.[45,46] Oxygen vacancy signals were then detected by ESR at $g = 2.00$ (Fig. S7†),[47] the calcined samples showed obvious signals of oxygen vacancies, whereas, $CaCl_2$/rutile TiO_2 did not show any single electron signal (Ti^{3+} or single electron trapped in oxygen vacancies), indicating the absence of defect sites in $CaCl_2$/rutile TiO_2. Even so, there are dislocations (line defects) in $CaCl_2$/rutile TiO_2, which should be responsible for the enhanced pre-peak B. Another change in normalized Ti K-edge XANES spectra is the absorption edge. It is easy to understand why the lower absorption edge energy of calcined samples stems from the existence of Ti^{3+}, while, the inconformity of the absorption edge of $CaCl_2$/rutile TiO_2 cannot be explained in terms of valence characteristics of Ti ions. Instead, the covalency in $CaCl_2$/rutile TiO_2 was enhanced due to the shortened Ti–O distance.

In addition, Ti $L_{2,3}$-edge absorption spectra are also measured to study the electronic structure, as shown in Fig. 3d. Two sets of local maxima over this energy range could be assigned to Ti $2p_{3/2}$ (L_3: peaks t_{2g} and e_g) and Ti $2p_{1/2}$ (L_2: peaks t_{2g} and e_g) core levels into empty Ti 3d states.[48,49] It should be noted that the difference value (ΔE) of peaks t_{2g} (L_3) to e_g (L_3) of $CaCl_2$/rutile TiO_2 decreases compared with other samples, which is caused by the lattice distortion of rutile TiO_2.

It is well known that the formation of TiO_2 in different phases (like rutile, anatase, and brookite) proceeds under specific conditions, and these phases often transform into each other through external energy, as previously reported.[50,51] However, $CaCl_2$ structured TiO_2 has not been obtained under mild conditions and the formation inducement has not been uncovered. Herein, we initiated experiments under a broad range of conditions with varying the amount of reactants and reaction temperature with an aim to obtain the phase diagram for given phases and nanostructures (Fig. 4a, S8 and S9†). It seems that solution reaction with a high concentration of $TiCl_4$ leads to the occurrence of $CaCl_2$-type structured TiO_2, while a low concentration of $TiCl_4$ causes an appearance of the anatase phase. In the boundary of the $CaCl_2$ phase and anatase phase, pure rutile formed. With increasing the amount of $TiCl_4$, no products could be obtained except for a solution. Through this mapping, we didn't find an indication that pure $CaCl_2$ phase TiO_2 is formed through the hydrolytic process of $TiCl_4$. This may be due to the metastable structure of $CaCl_2$ phase TiO_2, which makes it hard to stabilize by itself. Further, the symbiotic structure is vital in stabilizing the metastable $CaCl_2$ phase TiO_2. Based on the synthetic maps, the possible formation process of $CaCl_2$/rutile TiO_2 was proposed in terms of the schematic diagram in Fig. 4b: when the starting reactant $TiCl_4$ was dissolved in water, water-soluble precursor $Ti(OH)_2(OH_2)_4Cl_2$ was formed initially, and the solution became highly acidic. Then, the precursor was dissociated and condensed to crystallize TiO_2 through an oxolation. At a high concentration of $TiCl_4$, $Ti(OH)_2(OH_2)_4Cl_2$ could not be completely disintegrated to create a crystalline TiO_2 phase,[52] leaving lots of redundant saturation $Ti(OH)_2(OH_2)_4{}^{2+}$ ions and Cl^- ions scattered around the crystals that affect the crystallization and the subsequent grain growth process. Even after the reaction, there remained a great number of $Ti(OH)_2(OH_2)_4{}^{2+}$ ions in the solution. In order to verify the existence of soluble titanium compounds, the filter liquor was collected. At first, ultra-pure H_2O was added, the solution showed a phenomenon of liquid miscibility with visible flow traces, and no precipitates appeared, which is due to the large viscosity and mobility difference between H_2O and the filter liquor with a high concentration of $Ti(OH)_2(OH_2)_4{}^{2+}$. Then, excessive NaOH was put in and plenty of white precipitates appeared which indicates the presence of titanium compounds in this filter liquor. This observation shows that a high concentration of $Ti(OH)_2(OH_2)_4{}^{2+}$ ions plays an important role in the formation of symbiotic $CaCl_2$/rutile TiO_2. Similar cases have been reported elsewhere, in which ions can regulate the morphology and structure of final products.[53,54]

The stability of $CaCl_2$/rutile TiO_2 was measured using *in situ* XRD through increasing the temperature gradually. The double peak feature of plane (110) is still clear when calcined at temperatures <200 °C, and then fades away as the calcination temperature increases (Fig. 5a). Meanwhile, such a feature remains unchanged if the samples are kept at room temperature for as long as three years (Fig. 5c), suggesting a good stability. Clearly, in the phase transition process, the double peaks located at two theta of about 27.0° and 27.9° gradually change into a single peak at two theta of about 27.5° (Fig. 5b). This reflects the lattice change process more intuitively: the $CaCl_2$ phase fades away little by little, and the rutile phase contracts in the lattice with grain growth.

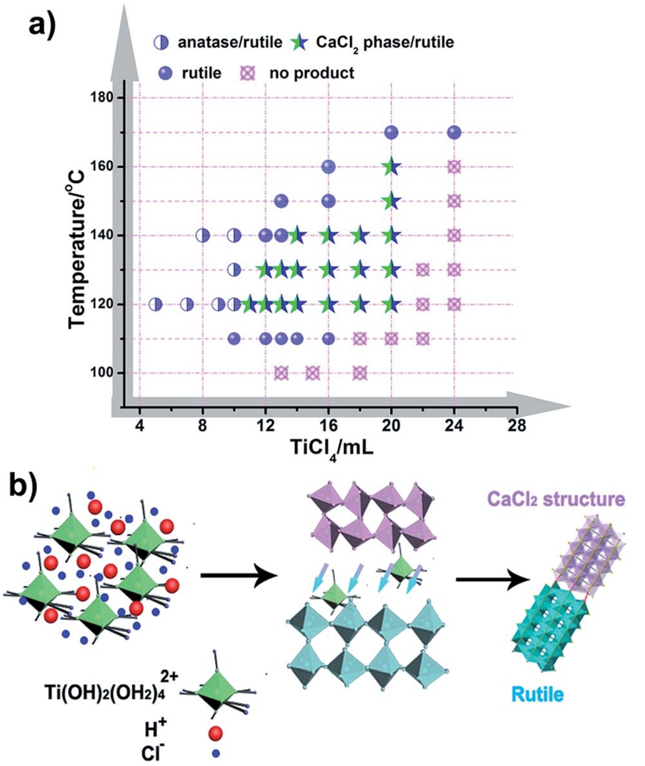

Fig. 4 Chemical synthesis routes. (a) Maps for the synthesis of TiO_2 at various hydrothermal temperatures and addition amounts of $TiCl_4$. (b) The synthetic schematic diagram for the formation of $CaCl_2$/rutile TiO_2.

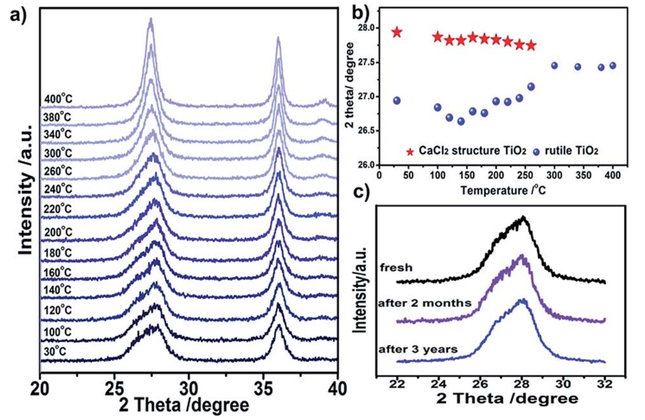

Fig. 5 Stability of symbiotic $CaCl_2$/rutile TiO_2. (a) *In situ* XRD patterns for $CaCl_2$/rutile TiO_2 with increasing temperature from 30 to 400 °C. (b) Peak position variation as temperature increases. (c) XRD patterns for fresh $CaCl_2$/rutile TiO_2 and the samples after being stored in air for two months and three years as well.

It is well known that hetero-nanocomposites of TiO_2 like P25 are excellent photocatalysts, however, no one knows what the performance is for symbiotic hetero-nanocomposite $CaCl_2$/rutile TiO_2. Since the band structure of $CaCl_2$-type TiO_2 directly determines its photocatalytic activity, we calculated the density of states (DOS) of $CaCl_2$ phase TiO_2 and rutile TiO_2 in $CaCl_2$/rutile TiO_2 (Fig. 6a). The conduction band minimum of both materials originates from the Ti 3d orbital, and the valence band maximum consists mainly of the O 2p orbital. Nevertheless, the band gap energy of $CaCl_2$ structured TiO_2 ($E_g \approx 3.3$ eV) is obviously larger than that of rutile TiO_2 ($E_g \approx 3.1$ eV). The origin of the difference in band structure lies in the unique features of $CaCl_2$ phase TiO_2, which owns an entirely different octahedral configuration and Ti–O bond length when compared to rutile TiO_2. The change in bond length could affect the interaction between orbitals, leading to variations in the band position.[55] Experimentally, we measured the diffuse reflectance ultraviolet-visible spectra and XPS valence band spectra. The absorbance range of $CaCl_2$/rutile TiO_2 is similar to that of rutile TiO_2 ($E_g \approx 3.1$ eV) except for an enhanced absorption intensity around 360 nm (Fig. S10†). Combined with the DOS analysis results in which the band gap of $CaCl_2$ phase TiO_2 is wider than that of rutile TiO_2, we could attribute the enhanced light absorption near 360 nm to the electron excitation from the O 2p orbital to the Ti 3d orbital of the $CaCl_2$ phase TiO_2. The edge absorption around 400 nm primarily originates from electron excitation from the O 2p orbital to the Ti 3d orbital of rutile TiO_2. From XPS spectra in Fig. S11,† the valence band of $CaCl_2$/rutile TiO_2 is determined to be about 0.2 eV lower than that of rutile TiO_2 ($E_{VBM}^{rutile} = 2.62$ eV, $E_{VBM}^{CaCl_2/rutile} = 2.44$ eV). Thus, $CaCl_2$/rutile TiO_2 forms a type II heterojunction similar to that of P25, as illustrated in the schematic diagram (Fig. 6f). Photoexcited charges would transport and accumulate in semiconductors.[56,57] That is, photo-generated electrons in $CaCl_2$ structured TiO_2 could transport to rutile TiO_2 preferentially to conduct reduction reactions. Meanwhile, the holes left in the valence of rutile TiO_2 would transport to $CaCl_2$ structured TiO_2 preferentially to react with the sacrificial agent.

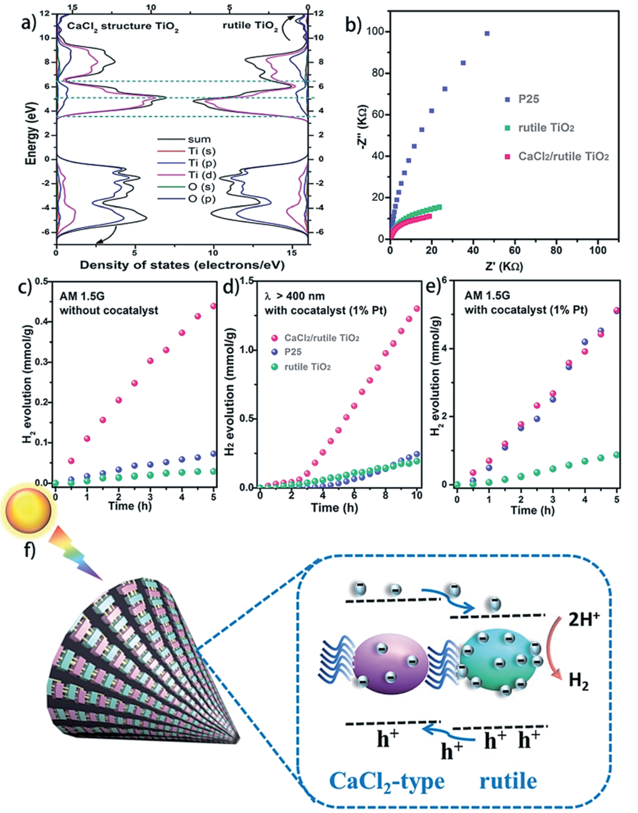

Fig. 6 Photocatalytic performance of $CaCl_2$/rutile TiO_2. (a) Calculated density of states (DOS) of $CaCl_2$ structured TiO_2 and rutile TiO_2; (b) Nyquist plots of the EIS for $CaCl_2$ structured TiO_2, P25, and commercial rutile TiO_2 (Ref.rutile); Water splitting hydrogen evolution activities for $CaCl_2$/rutile TiO_2, commercial rutile TiO_2 (Ref.rutile), and P25: (c) without any cocatalyst under simulated sunlight (with an AM 1.5G filter), (d) with the assistance of 1% Pt as the cocatalyst under simulated sunlight (with an AM 1.5G filter) and (e) visible light (wavenumber > 400 nm) illumination. (f) Schematic diagram for the electron transfer process under the illumination of light for $CaCl_2$/rutile TiO_2.

The charge separation and transport efficiency were evaluated through electrochemical impedance measurements (EIS). As shown in Fig. 6b, the arc in the low-frequency range originates from electron transfer resistance (R_t). Obviously, the arc of $CaCl_2$/rutile TiO_2 is smaller than those of Ref.TiO_2 and P25, indicating a more rapid electron transfer process in $CaCl_2$/rutile TiO_2. As expected, the as-prepared $CaCl_2$/rutile TiO_2 exhibits a superior performance in mass-specific H_2 evolution (1024 μmol g^{-1} h^{-1}) to rutile TiO_2 (174 μmol g^{-1} h^{-1}), and a comparable performance with P25 (1019 μmol g^{-1} h^{-1}) under AM 1.5G simulated sunlight with the assistance of 1% Pt cocatalyst (Fig. 6e). It is well known that P25 is an excellent ultraviolet light absorber, while its visible light absorbance ability is low. Comparatively, the absorption edge of $CaCl_2$/rutile TiO_2 showed an obvious red shift compared with P25, which means that $CaCl_2$/rutile TiO_2 owns a wider range of light absorption (Fig. S10†). Besides this, dislocations that involve defects and/or local disorder may provide a mid-gap state in $CaCl_2$/rutile TiO_2 to broaden the light absorption range.[58] Thus, under visible light illumination ($\lambda > 400$ nm), $CaCl_2$/rutile TiO_2 exhibited the highest H_2 evolution activity (177 μmol g^{-1} h^{-1}), much higher than that of commercial rutile TiO_2 (23 μmol g^{-1} h^{-1}) and P25 (42 μmol g^{-1} h^{-1}) (Fig. 6d). Surprisingly, without the assistance of a cocatalyst, $CaCl_2$/rutile TiO_2 still showed the most outstanding performance under the illumination of simulated sunlight (Fig. 6c), which also indicates the excellent charge separation ability of symbiotic $CaCl_2$/rutile TiO_2. The cycle tests of $CaCl_2$/rutile TiO_2 for photocatalytic H_2 generation proved a high stability in performance (Fig. S12†), which is further confirmed by the maintained structural feature after photocatalytic tests (Fig. S13†). Such an excellent performance can be primarily attributed to (i) the special structure of $CaCl_2$-phase TiO_2 which provides the $CaCl_2$/rutile TiO_2 hetero-nanocomposite with a higher reduction ability, and (ii) the symbiotic relationship that allows the $CaCl_2$/rutile TiO_2 hetero-nanocomposite to show a strong interaction, which could separate and transport carriers efficiently.

TiO_2 is a multipurpose material, and many efforts have been made investigating the microwave absorption and terahertz absorption performance of hydrogenated TiO_2.[59,60] Thus, we examined the microwave absorption performance (1–18 GHz) of $CaCl_2$/rutile TiO_2, Ref.TiO_2 and P25 (Fig. S14 and S15†). Compared with Ref.TiO_2 and P25, $CaCl_2$/rutile TiO_2 improved the reflection loss or absorption of the microwave irradiation (see details in the ESI†). This is likely from the existence of $CaCl_2$ phase TiO_2. There are also many other potential applications worth studying, and the symbiotic $CaCl_2$/rutile TiO_2 hetero-nanocomposite is believed to be a promising candidate in other areas.

Conclusions

We report the synthesis of a symbiotic $CaCl_2$/rutile TiO_2 hetero-nanocomposite through a facile hydrothermal approach. The successful synthesis relies on the existence of high concentration $Ti(OH)_2(OH_2)_4^{2+}$, which affects nucleation and crystallization behaviour, resulting in the formation of $CaCl_2$ structured TiO_2 intergrown with rutile TiO_2. In this composite, orthorhombic $CaCl_2$ phase TiO_2 with a space group of *Pnnm* was stabilized by tetragonal phase rutile nanocrystals through dislocation connection in between both structures. Such a symbiotic relationship leads to a type II heterojunction, which enhances the charge separation and transport ability. The specific structure of $CaCl_2$/rutile TiO_2 elevated the reduction capacity, enabling a superior photocatalytic water splitting activity higher than that of the most widely used photocatalyst P25. We believe that the synthesis of the symbiotic $CaCl_2$/rutile TiO_2 hetero-nanocomposite reported here would facilitate its extensive research in those fields that have not yet been found and would provide guidance for the synthesis of other advanced hetero-nanocomposite materials.

Conflicts of interest

The authors declare no competing financial interest.

Acknowledgements

We acknowledge the technical assistance of the Beijing Synchrotron Radiation Facility (BSRF) and National Synchrotron Radiation Laboratory (NSRL), Hefei, China. We also thank Pro. Xiaolong Wang (Jilin University), Pro. Minqiang Wang (Xi'an Jiaotong University), Dr Song Xia (Xi'an Jiaotong University), and Dr Xiangli Che (Shanghai Institute of Silicate, Chinese Academy of Sciences) for their assistance with the measurement and analysis of microwave absorption. This research is supported by the financial assistance of NSFC (21671077, 21871106, 21571176, and 21771075) and Interdisciplinary Research Grant for PhDs of Jilin University (10183201816).

Notes and references

1 C. Xia, Y. X. Cai, Y. Ma, B. Y. Wang, W. Zhang, M. Karlsson, Y. Wu and B. Zhu, *ACS Appl. Mater. Interfaces*, 2016, **8**, 20748–20755.

2 C. L. Tan and H. Zhang, *J. Am. Chem. Soc.*, 2015, **137**, 12162–12174.

3 H. Y. Wang, H. S. Yin, H. Huang, K. L. Li, Y. L. Zhou, G. I. N. Waterhouse, H. Lin and S. Y. Ai, *Biosens. Bioelectron.*, 2018, **108**, 89–96.

4 G. Chen, Y. Zhao, G. Fu, P. N. Duchesne, L. Gu, Y. Zheng, X. Weng, M. Chen, P. Zhang, C. W. Pao, J. F. Lee and N. Zheng, *Science*, 2014, **344**, 495–499.

5 B. Kong, J. Tang, Y. Zhang, T. Jiang, X. Gong, C. Peng, J. Wei, J. Yang, Y. Wang, X. Wang, G. Zheng, C. Selomulya and D. Zhao, *Nat. Chem.*, 2016, **8**, 171–178.

6 J. Cai, M. Wu, Y. Wang, H. Zhang, M. Meng, Y. Tian, X. Li, J. Zhang, L. Zheng and J. Gong, *Chem*, 2017, **2**, 877–892.

7 X. Y. Zheng, C. K. Yang, X. H. Chang, T. Wang, M. Ye, J. Lu, H. H. Zhou, J. Zheng and X. G. Li, *Adv. Mater.*, 2018, **30**, 1704353.

8 D. Jung, L. M. A. Saleh, Z. J. Berkson, M. F. El-Kady, J. Y. Hwang, N. Mohamed, A. I. Wixtrom, E. Titarenko, Y. Shao, K. McCarthy, J. Guo, I. B. Martini, S. Kraemer, E. C. Wegener, P. Saint-Cricq, B. Ruehle, R. R. Langeslay, M. Delferro, J. L. Brosmer, C. H. Hendon, M. Gallagher-Jones, J. Rodriguez, K. W. Chapman, J. T. Miller, X. Duan, R. B. Kaner, J. I. Zink, B. F. Chmelka and A. M. Spokoyny, *Nat. Mater.*, 2018, **17**, 341–348.

9 M. Zhu, Z. Sun, M. Fujitsuka and T. Majima, *Angew. Chem., Int. Ed.*, 2018, **57**, 2160–2164.

10 Y. P. Zang, L. P. Li, Y. S. Xu, Y. Zuo and G. S. Li, *J. Mater. Chem. A*, 2014, **2**, 15774–15780.

11 B.-R. Wulan, S.-S. Yi, S.-J. Li, Y.-X. Duan, J.-M. Yan and Q. Jiang, *Appl. Catal., B*, 2018, **231**, 43–50.

12 Q. Li, F. Zhao, C. Qu, Q. Shang, Z. Xu, L. Yu, J. R. McBride and T. Lian, *J. Am. Chem. Soc.*, 2018, **140**, 11726–11734.

13 B. Dong, J. Cui, Y. Gao, Y. Qi, F. Zhang and C. Li, *Adv. Mater.*, 2019, e1808185.

14 X. Chen, L. Li, Y. Xu, Y. Zhang and G. Li, *RSC Adv.*, 2016, **6**, 995–1003.

15 Y. Suchorski, S. M. Kozlov, I. Bespalov, M. Datler, D. Vogel, Z. Budinska, K. M. Neyman and G. Rupprechter, *Nat. Mater.*, 2018, **17**, 519–522.

16 H. Jeong, J. Bae, J. W. Han and H. Lee, *ACS Catal.*, 2017, **7**, 7097–7105.

17 I. X. Green, W. Tang, M. Neurock and J. T. Yates Jr, *Science*, 2011, **333**, 736–739.

18 M. Shahidi, B. Pichler and C. Hellmich, *Acta Mech.*, 2016, **227**, 229–252.

19 V. Thery, A. Boulle, A. Crunteanu, J. C. Orlianges, A. Beaumont, R. Mayet, A. Mennai, F. Cosset, A. Bessaudou and M. Fabert, *Phys. Rev. B*, 2016, **93**, 184106.

20 H. Liang, Q. Meng, X. Wang, H. Zhang and J. Wang, *ACS Appl. Mater. Interfaces*, 2018, **10**, 14145–14152.

21 H. Liu, W. Li, D. Shen, D. Zhao and G. Wang, *J. Am. Chem. Soc.*, 2015, **137**, 13161–13166.

22 M. M. Shi, D. Bao, B. R. Wulan, Y. H. Li, Y. F. Zhang, J. M. Yan and Q. Jiang, *Adv. Mater.*, 2017, **29**, 1606550.

23 J. C. Perez-Flores, C. Baehtz, A. Kuhn and F. Garcia-Alvarado, *J. Mater. Chem. A*, 2014, **2**, 1825–1833.

24 H. Razavi-Khosroshahi, K. Edalati, M. Hirayama, H. Emami, M. Arita, M. Yamauchi, H. Hagiwara, S. Ida, T. Ishihara, E. Akiba, Z. Horita and M. Fuji, *ACS Catal.*, 2016, **6**, 5103–5107.

25 A. Escudero, L. Delevoye and F. Langenhorst, *J. Phys. Chem. C*, 2011, **115**, 12196–12201.

26 A. Escudero and F. Langenhorst, *J. Solid State Chem.*, 2012, **190**, 61–67.

27 J. Zhang, L. P. Li, X. S. Huang and G. S. Li, *J. Mater. Chem.*, 2012, **22**, 10480–10487.

28 K. Suito, N. Kawai and Y. Masuda, *Mater. Res. Bull.*, 1975, **10**, 677–680.

29 Y. Tsuchida and T. Yagi, *nature*, 1989, **340**, 217–220.

30 J. Haines, J. M. Leger and C. Chateau, *Phys. Rev. B: Condens. Matter Mater. Phys.*, 2000, **61**, 8701–8706.

31 S. Ono and K. Mibe, *Phys. Rev. B: Condens. Matter Mater. Phys.*, 2011, **84**, 054114.

32 N. Stojilovic, *J. Chem. Educ.*, 2018, **95**, 598–600.

33 S. Pereira, M. R. Correia, E. Pereira, K. P. O'Donnell, R. W. Martin, M. E. White, E. Alves, A. D. Sequeira and N. Franco, *Mater. Sci. Eng., B*, 2002, **93**, 163–167.

34 M. J. Shearer, L. Samad, Y. Zhang, Y. Zhao, A. Puretzky, K. W. Eliceiri, J. C. Wright, R. J. Hamers and S. Jin, *J. Am. Chem. Soc.*, 2017, **139**, 3496–3504.

35 H. Huang, H. Jia, Z. Liu, P. Gao, J. Zhao, Z. Luo, J. Yang and J. Zeng, *Angew. Chem., Int. Ed.*, 2017, **56**, 3594–3598.

36 D. B. Varshney, J. A. Elliott, L. A. Gatlin, S. Kumar, R. Suryanarayanan and E. Y. Shalaev, *J. Phys. Chem. B*, 2009, **113**, 6177–6182.

37 J. Hafizovic, M. Bjorgen, U. Olsbye, P. D. C. Dietzel, S. Bordiga, C. Prestipino, C. Lamberti and K. P. Lillerud, *J. Am. Chem. Soc.*, 2007, **129**, 3612–3620.

38 K. M. Jensen, M. Christensen, P. Juhas, C. Tyrsted, E. D. Bojesen, N. Lock, S. J. Billinge and B. B. Iversen, *J. Am. Chem. Soc.*, 2012, **134**, 6785–6792.

39 O. Frank, M. Zukalova, B. Laskova, J. Kurti, J. Koltai and L. Kavan, *Phys. Chem. Chem. Phys.*, 2012, **14**, 14567–14572.

40 T. Lan, X. Tang and B. Fultz, *Phys. Rev. B: Condens. Matter Mater. Phys.*, 2012, **85**, 094305.

41 S. Zhou, E. Čižmár, K. Potzger, M. Krause, G. Talut, M. Helm, J. Fassbender, S. A. Zvyagin, J. Wosnitza and H. Schmidt, *Phys. Rev. B: Condens. Matter Mater. Phys.*, 2009, **79**, 113201.

42 J. C. Parker and R. W. Siegel, *Appl. Phys. Lett.*, 1990, **57**, 943–945.

43 V. Swamy, *Phys. Rev. B: Condens. Matter Mater. Phys.*, 2008, **77**, 195414.

44 C. Ribeiro, C. Vila, D. B. Stroppa, V. R. Mastelaro, J. Bettini, E. Longo and E. R. Leite, *J. Phys. Chem. C*, 2007, **111**, 5871–5875.

45 C. X. Kronawitter, J. R. Bakke, D. A. Wheeler, W. C. Wang, C. Chang, B. R. Antoun, J. Z. Zhang, J. Guo, S. F. Bent, S. S. Mao and L. Vayssieres, *Nano Lett.*, 2011, **11**, 3855–3861.

46 J. Wan, W. Chen, C. Jia, L. Zheng, J. Dong, X. Zheng, Y. Wang, W. Yan, C. Chen, Q. Peng, D. Wang and Y. Li, *Adv. Mater.*, 2018, **30**, 1705369.

47 L. Li, J. Yan, T. Wang, Z. J. Zhao, J. Zhang, J. Gong and N. Guan, *Nat. Commun.*, 2015, **6**, 5881.

48 G. C. Vásquez, S. Z. Karazhanov, D. Maestre, A. Cremades, J. Piqueras and S. E. Foss, *Phys. Rev. B*, 2016, **94**, 235209.

49 S. O. Kucheyev, T. van Buuren, T. F. Baumann, J. H. Satcher, T. M. Willey, R. W. Meulenberg, T. E. Felter, J. F. Poco, S. A. Gammon and L. J. Terminello, *Phys. Rev. B: Condens. Matter Mater. Phys.*, 2004, **69**, 245102.

50 W. Hu, L. Li, G. Li, Y. Liu and R. L. Withers, *Sci. Rep.*, 2014, **4**, 6582.

51 W. Hu, L. Li, W. Tong and G. Li, *Chem. Commun.*, 2010, **46**, 3113–3115.

52 H. Lin, L. Li, M. Zhao, X. Huang, X. Chen, G. Li and R. Yu, *J. Am. Chem. Soc.*, 2012, **134**, 8328–8331.

53 Y. Liu, J. Wei, Y. Tian and S. Yan, *J. Mater. Chem. A*, 2015, **3**, 19000–19010.

54 J. Ning, Q. Dai, T. Jiang, K. Men, D. Liu, N. Xiao, C. Li, D. Li, B. Liu, B. Zou, G. Zou and W. W. Yu, *Langmuir*, 2009, **25**, 1818–1821.

55 R. Kuriki, T. Ichibha, K. Hongo, D. Lu, R. Maezono, H. Kageyama, O. Ishitani, K. Oka and K. Maeda, *J. Am. Chem. Soc.*, 2018, **140**, 6648–6655.

56 T. Xia, N. Li, Y. Zhang, M. B. Kruger, J. Murowchick, A. Selloni and X. Chen, *ACS Appl. Mater. Interfaces*, 2013, **5**, 9883–9890.

57 L. Guan and X. Chen, *ACS Appl. Energy Mater.*, 2018, **1**, 4313–4320.

58 X. Chen, L. Liu, P. Y. Yu and S. S. Mao, *Science*, 2011, **331**, 746–750.

59 M. A. Green, J. Xu, H. Liu, J. Zhao, K. Li, L. Liu, H. Qin, Y. Zhu, D. Shen and X. Chen, *Mater. Today Phys.*, 2018, **4**, 64–69.

60 T. Xia, C. Zhang, N. A. Oyler and X. Chen, *Adv. Mater.*, 2013, **25**, 6905–6910.